Chapter 8

RE_2O_3 Nanoparticles Embedded in SiO_2 Glass Matrix — A Colossal Dielectric and Magnetodielectric Response

S. Mukherjee, T. H. Kao, H. C. Wu, K. Devi Chandrasekhar and H. D. Yang

Additional information is available at the end of the chapter

http://dx.doi.org/10.5772/60677

Abstract

Significant experimental effort has been inspected to consider and implement favorable high-*k* gate dielectrics with magnetodielectric (MD) effect of series of rare earth oxide (RE_2O_3, RE ~ rare earth ions) nanoparticles (NPs) embedded in sol–gel derived SiO_2 glass matrix. Properly calcined RE_2O_3 NP-glass composite systems (in which RE ~ Sm, Gd and Er) show an intriguing colossal enhancement of dielectric constant along with MD effect near room temperature. The enhancement of dielectric constant is closely related to oxygen vacancy induced dielectric relaxation (or, more correctly, particle size effect from different calcined temperature), reconstructed from extended X-ray absorption fine structure. The MD response is strongly depended on the superparamagnetic property of the rare earth ions. From application point of view, the enhancement of dielectric constant associated with MD response can be achieved by tuning the NPs size through varying annealing temperature and/or increasing the doping concentration of magnetic rare earth oxide, which will be the key guidelines to accomplish the compatibility, performance and reliability requirements for future complementary metal-oxide-semiconductor (CMOS) technology.

Keywords: Rare earth oxide nanoparticle, high-*k* materials, magnetodielectric effect, diffuse phase transition

1. Introduction

Tiny electrical components are now unanimously required to be high in functionality and reliability and low priced in response to progress in the high density mounting technology.

Continued device scaling for future technology nodes requires reduction in equivalent oxide thickness (EOT) of gate dielectrics to maintain electrostatic control of the charges induced in the channel. The use of amorphous SiO_2 as a gate dielectric offers several key advantages in complementary metal-oxide semiconductor (CMOS) processing, including thermal and chemical stability as well as superior electrical isolation properties (high band gap of nearly 9 eV, and a Si–SiO_2 potential barrier for electrons of about 3 eV). The continuous miniaturization of Si electronics has imposed severe constraints on the performance of the SiO_2 gate oxide, with its thickness now approaching the quantum tunneling limit [1,2]. To continue the downward scaling, dielectrics with a higher dielectric constant (high-*k*) are being suggested as a solution to achieve the same transistor performance while maintaining a relatively thick physical thickness. Following this roadway, many materials systems (viz. lead–free non-ferroelectric) are currently under consideration as alternatives to conventional silicon oxide films as the gate dielectric material for sub-0.1 μm CMOS technology. Such an approach allows one to employ the best available materials for each phase, whose properties are known a priority due to the scarcity of high-*k* materials, to suit the desired application. Recent reports of giant dielectric constant have directed considerable attention to several new material systems, such as perovskite–related materials $ACu_3Ti_4O_{12}$ (A = Ca, $Bi_{2/3}$, $Y_{2/3}$, $La_{2/3}$) [3,4], $La_{2/3}Li_xTi_{1-x}Al_xO_3$ [5], Nd_2O_3 doped $(1-x)Bi_{0.5}Na_{0.5}TiO_{3-x}Bi_{0.5}K_{0.5}TiO_3$ [6], Fe-containing complex perovskites $A(Fe_{1/2}B_{1/2})O_3$ (A = Ba, Sr, Ca; B = Nb, Ta, Sb) [7,8], non-perovskite material $Li_{0.05}Ti_{0.02}Ni_{0.93}O$ [9], percolative $BaTiO_3$-Ni composites [10], electron-doped manganites $Ca_{1-x}La_xMnO_3$ and hole-doped insulators $La_2Cu_{1-x}Li_xO_4$ and $La_{2-x}Sr_xNiO_4$ [11–13]. The sensitivity of these complex oxides to strain, stoichiometry, phase heterogeneities, oxidation state, disorder, etc. can lead to drastic modifications in their magnetic and electric properties at the nanoscale. Besides that, as the key guidelines for replacing alternative dielectrics with high-*k* materials are required to (i) remain thermodynamically and chemically stable between the metal-oxide and Si substrate; (ii) kinetic stability against Si and the metal gate, in particular during high temperature processing and annealing; (iii) insulating properties: band offsets with Si over 1 eV to assure low leakage currents; (iv) a passivated, low-defect-density interface with Si to ensure large carrier mobility in the Si channel and good breakdown properties; and (v) interface quality between the high-*k* dielectrics and Si substrate: a low defect density in the high-*k* dielectric itself to prevent flat band and threshold voltage shifts and instabilities. Many dielectrics appear favorable in some of these areas, but very few materials are promising with respect to all of these guidelines. The ranking of HfO_2-based system as a desired high-*k* gate dielectric material to replace amorphous SiO_2 drops considerably, as HfO_2 suffers crystallization at a relatively low process temperature (< 500°C), resulting high leakage current along the grain boundaries [14]. Therefore, the exploitation of new type of amorphous phase pure high-*k* gate dielectrics candidates as a replacement of SiO_2 still faces several daunting challenges.

Besides the aforementioned consideration, the superior electrical characteristics of the Si–SiO_2 interface in ideal gate dielectric stack compatible with planarization technology has not achieved with any other alternative semiconductor–dielectric combination. Despite several key advantages of SiO_2, the continual scaling of CMOS technologies has pushed the Si–SiO_2 system in formidable challenge. One promising alternative approach to overcome the scaling limit has been proposed to substitute by silica-based single-valence nanoparticles (NPs) as gate

http://dx.doi.org/10.5772/60677

insulator (interface between silicon and NP-oxides embedded silica), where flexibility, compartibility and functionality may be achieved through different NPs sizes/concentrations. Concentrating on the desired NP-oxides, potentially stable rare earth oxides (RE_2O_3, RE ~ rare earth, a series of elements from La to Lu with stable RE^{3+}) were chosen, which are attractive materials based on good thermodynamic energy considerations with silicon, highly resistive and a high conduction band offset over 2 eV. We have presented extensive results, providing useful insight into the physics of nano-composite high-*k* gate dielectrics. Sol–gel derived non-magnetic SiO_2 glass matrix with magnetic/nonmagnetic rare earth NP-oxides provides a convenient way to tailor desired magnetic, dielectric (in presence of applied magnetic field), and other properties by altering the type, size and concentration of the dopant ions.

2. Sample preparation

The preparation of RE_2O_3:SiO_2 nano-glass composite system (RE ~ La, Nd, Sm, Eu, Gd, Dy, Ho, Er, Tm, Yb and Lu) consists of three consecutive processes: (a) preparation of wet gel in which rare earth ions were doped by sol–gel way, (b) drying of the gel and (c) densification of the dry gel to a dense glass in which RE_2O_3 NPs embedded by calcining at selective temperatures [15]. The process was based on the hydrolysis of precursors, such as tetraethylorthosilicate {$Si(OC_2H_5)_4$} (TEOS) and subsequent condensation of hydrolyzed TEOS in a medium containing a hydroalcoholic solution of rare earth salt [16] (Figure 1(a)) having different mol% concentrations following essentially the method developed by Sakka and Kamiya [17]. Water was required for the hydrolysis. The molar ratio of water and TEOS was kept at 20 while that of TEOS and catalyst HCl at 100. Dry ethanol was used for diluting the alkoxide. The following composition of the $Si(OC_2H_5)_4$ solutions used in the study (Table 1):

$Si(OC_2H_5)4$ (gm)	H_2O (gm)	C_2H_5OH (gm)	Mole ratio of H_2O to $Si(OC_2H_5)_4$	Volume	SiO_2 content (gm/100 cc)
169.5	292.8	37.5	20	500	9.80

Table 1. Compositions of the $Si(OC_2H_5)_4$ (TEOS), H_2O, and C_2H_5OH solutions used in the sol–gel process.

There are two distinct chemical reactions involved in the sol–gel process, describing Eqn. (1) for hydrolysis of the alcohol groups, Eqns. (2) and (3) for polycondensation of hydroxyl groups.

a. Hydrolysis:

$$\equiv \text{Si-OR} + H_2O \rightarrow \equiv \text{Si-OH} + \text{ROH} \tag{1}$$

b. Condensation (water/alcohol condensation):

i. Water condensation:

$$\equiv \text{Si-OH} + \equiv \text{Si-OH} \rightarrow \equiv \text{Si-O-Si} \equiv + H_2O \tag{2}$$

Alcohol condensation:

$$\equiv \text{Si-OH} + \equiv \text{Si-OR} \rightarrow \equiv \text{Si-O-Si} \equiv + \text{ROH} \tag{3}$$

The clear solutions without any precipitaion are prepared with the mixing of half amount of ethanol in alkoxide and the solution consisting of the specified amount of water with another half of the ethanol containing HCl and dopant. The mixure solutions continued stirring for 2–3 hours at room temperature. The clear solution was kept in pyrex beaker at the atmospheric condition for 7/8 days to form stiff monolithic transparent gel. Further, the gels were allowed to dry for 4–5 weeks at room temperature. The dried (liquid removed by thermal evaporation) monolith is termed as xerogel. The oven–dried gel (temperature range 100–200°C) still contains large concentration of chemisorbed hydroxyls. Heat treatment in the temperature range 500–800°C desorbs the hydroxyls, forming a stabilized gel. At 1000°C, it transformed to a dense glass. Heat treatments of samples were performed according to preselected calcination temperature schedule [16] (Figure 1(b)).

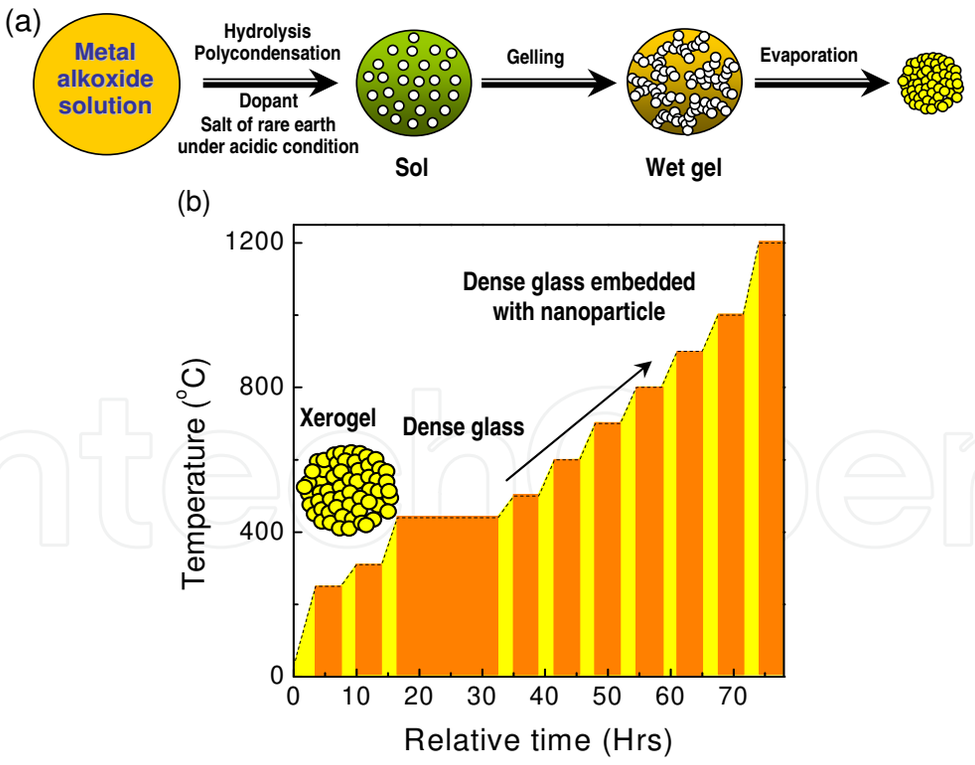

Figure 1. (Color online) (a) Sol–gel process. (b) Gel–glass embedded with rare earth nanoparticle calcination process.

It is relevant to mention here the important findings of Raman spectroscopic studies including measurements of pore size, density and specific surface area on the densification of undoped

http://dx.doi.org/10.5772/60677

SiO_2 gel as a function of heat treatment up to 900°C [18]. With increasing temperature from 700 to 800°C, the average pore size increases abruptly from 1.0 nm to 2.3 nm, whereas, the specific surface area decreases from 550 m^2/g to 160 m^2/g and the pore volume/gm decreases from 0.19 cc/g to 0.12 cc/g. The surface energy for a siloxane surface is higher than for a hydroxyl surface. The Si–OH groups condense to Si–O–Si bonds with increasing temperature, thus increasing the surface energy as well as enhancing pore collapse. In these rare earth elements doped gel-glass specimens, a large number of small pores collapse at 700°C and an agglomeration of individual RE^{3+} are set free after small pores collapse to form NPs. The remaining pores join to form larger pores. At still higher temperature (i.e., 800°C), collapse of larger pores also takes place with similar observation in undoped sample, which is indicated by rapid fall of pore volume/g from 0.12 cc/g to 0.026 cc/g in going from 800°C to 900°C [18]. Thus it is possible at the highest temperature in the present case (i.e., 1200°C), the rare earth oxide NPs grow to a maximum size because of complete annihilations of pores, leading to a disappearance of Si – OH groups to condensation of Si–O–Si bonds. To this end, we have systematically synthesized nano-glass composites systems with different doping concentrations of rare earth elements to prepare the sols, since the gelation process (rate of the hydrolysis and condensation reactions) strongly affect with varying the kind and/or the amount of the starting solvent and the final outcome of the preparation.

3. Experimental details

Powder X-ray diffraction (XRD) of the sample was performed by using Cu- K_α radiation. To analyze the detailed structure of samples, an ultrahigh-resolution transmission electron microscopy (TEM) (Model: JEM-3010, JEOL) was employed of NPs embedded SiO_2 glass matrix calcined at different temperatures. Impedance spectroscopic measurements with/without magnetic field are carried out in the temperature range 150–350 K using LCR meter (Model E4980A, Agilent) in conjunction with laboratory built cryostat arrangement integrated to the physical properties measurement system (Model: 6000, Quantum Design). The magnetization (zero-field-cooled and field-cooled conditions) and magnetic hysteresis measurements are performed using a SQUID magnetometer (Model: MPMS-XL, Quantum Design) with temperatures varying from 2 to 350 K with ±1.0 K thermal stability and equipped with a superconducting magnet producing fields up to ±60 kOe. The sample in the powder form was packed in polytetrafluoroethylene (PTFE) capsule, where sample mass was chosen in the range of 8 to 12 mg for obtaining a good signal-to-noise ratio. Room temperature extended X-ray absorption fine structure (EXAFS) experiments were carried out in fluorescence mode (very low concentration of RE^{3+}) at the RE ~ Er/Gd/La L_{III}-edge at the 17C beamline in the National Synchrotron Radiation Research Center (NSRRC), Hsinchu, Taiwan. The EXAFS analysis was based on a multiparameter single-scattering fit (by the FEFFIT code [19] and using standard IFEFFIT data analysis package) in the *R*-space from the first two coordination shells; the fitting in the *k*-space (k^2-weighted $\chi(k)$ with a *k*-cut range from 2.5-8 $Å^{-1}$) led to the same result. A reference sample of bulk RE_2O_3 (unsupported SiO_2 glass matrix) was used as a model standard for determining co-ordination numbers and inter-atomic distances. In obtaining the EXAFS

function $\chi(k)$, the background absorption features which were superimposed on the EXAFS oscillations were removed from the spectrum using spline fit to both the pre-edge and the post-edge regions.

4. Results and discussion

A. Structural studies through transmission electron microscopy (TEM) and X-ray diffraction (XRD): Typical data are shown for Er_2O_3:SiO_2 NPs-glass composite system having 0.5 mol% dopant Er_2O_3 concentration calcined at different temperatures, namely, 700, 800, 900, and 1200°C (henceforth referred as Er05-7, Er05-8, Er05-9 and Er05-12, respectively) [20]. Here, we discuss the TEM image of the powder specimen of typical Er05-8 (Figure 2(a)), showing nearly spherical NPs of Er_2O_3 embedded in the glass matrix in the range of 3–6 nm. The particle size distributions histogram (upper inset of Figure 2(a)) of the sample is calculated by counting onto the the micrograph at least 100 particles from Figure 2. The high-resolution TEM (HRTEM) image (lower inset of Figure 2(a)) of the respective sample also shows lattice fringes with interplanar spacing (3.04 Å). The selected area electron diffraction (SAED) pattern (Figure 2(b)) also shows spotted ring patterns, developing the regions of localized crystallinity.

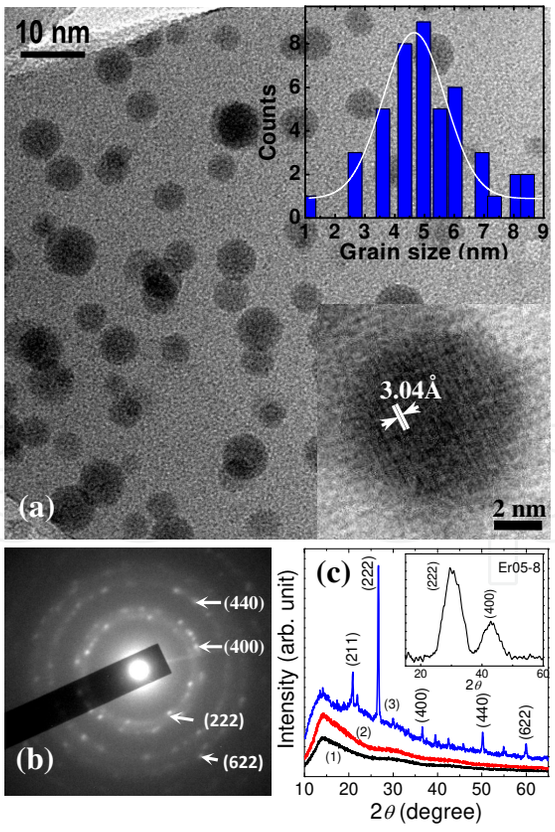

Figure 2. (Color online) (a) TEM image of Er05-8, upper inset: the particle size distribution histogram and lower inset: the HRTEM image, (b) electron diffraction and (c) XRD patterns of all the Er05-7, Er05-8 and Er05-12 samples.

http://dx.doi.org/10.5772/60677

The XRD patterns of the Er_2O_3 oxide NPs doped SiO_2 matrix calcined at 1200°C (Er05-12) show crystalline nature with quite large Er_2O_3 NPs. It exhibits clearly in Figure 2(c) the most intense characteristic line of single phase Er_2O_3 (JCPDF Card No. 43-1007) at 2θ~ 29.30° (222) corresponding the unit cell parameter a = 10.54 Å (space group: *Ia3*(206)). The sizes of Er-oxide NPs in Er05-12 are also estimated (> 40 nm) by applying the well-known Scherrer's equation from the integral breadths of the XRD lines. XRD patterns cannot be well resolved from feeble broad peaks due to their amorphous-like character of Er05-7 and Er05-8 samples. However, it is significantly mentioned here that the sizes of Er_2O_3 NPs grow larger for samples calcined at higher temperatures. In the SiO_2 glass matrix, low concentrations of Er^{3+} ions are bound to non-bridging oxygen atoms with quite low solubility [21]. Consequently, at a higher Er_2O_3 concentration with SiO_2 (1:2), the formation of an $Er_2Si_2O_7$ mixture with Er_2O_3 may occur at 1200°C [22]. However, at a higher calcined temperature (~1200°C and above), there is a possibility of the formation of $Er_2Si_2O_7$ mixture with crystalline Er_2O_3 even with very low concentration (0.5 mol %) of dopant ions. Herein, the sample obtained at 1200°C are not emphasized because of the observed dielectric behavior (discussed in the next section) is almost comparable with pure bulk Er_2O_3 (unsupported with SiO_2).

B. Dielectric and magnetodielectric (MD) effect

Er_2O_3 NPs-glass composite system: colossal enhancement of dielectric constant and large MD effect

Among various rare earth oxides, Er_2O_3 has been chosen first in the present work as it possesses most appealing properties viz. high resistivity (10^{12}-10^{15} cm^{-3}), large band gap (E_g= 5–7 eV), static dielectric constant (k ~ 14) [23,24], good thermodynamic stability with silicon and, moreover, not yet been explored from the viewpoint of observing the high MD effect. Although, present TEM and XRD studies also stimulate us for further exhaustive investigation on typical Er_2O_3:SiO_2 nano-glass composite system with different Er_2O_3 NPs size to throw more light exploring the origin and application feasibility on these rich dielectric materials. Typical data are shown for a Er_2O_3:SiO_2 nano-glass composite system having 0.5 mol% dopant (Er_2O_3) concentration calcined at different temperatures, namely, 700, 800, 900, and 1200°C (henceforth referred as Er05-7, Er05-8, Er05-9 and Er05-12 respectively).

4.1. Temperature dependence dielectric response

Figure 3(a) illustrates the relative dielectric constant (ε') vs. temperature curves of typical Er05-8 sample without applied magnetic field measured at several selective frequencies (1–100 kHz). The shape of the curves with a notable broadening around the well-defined maxima ε'_m (maximum value of ε') is indicative of a diffuse phase transition (DPT) presence [25-27] with high ε' (~ 600 at 1 kHz), quite different from and much higher than pure bulk Er_2O_3 (ε' ~ 11.5) [28] and SiO_2 (ε' ~ 3.9). Following the concept of DPT, the dielectric constant accords with a modified Curie–Weiss type equation viz. $\varepsilon'^{-1} - \varepsilon'^{-1}_m = C_i(T - T_m)^\gamma$, where γ is the diffuseness exponent indicative of degree of disorder, C_i is a temperature independent coefficient (in general, dependent of frequency) and ε'_m is the maximum value of ε' at T_m. For γ = 1, normal Curie–Weiss behavior and γ ~ 2, it implies typical DPT for the ideal ferroelectric relaxor [29].

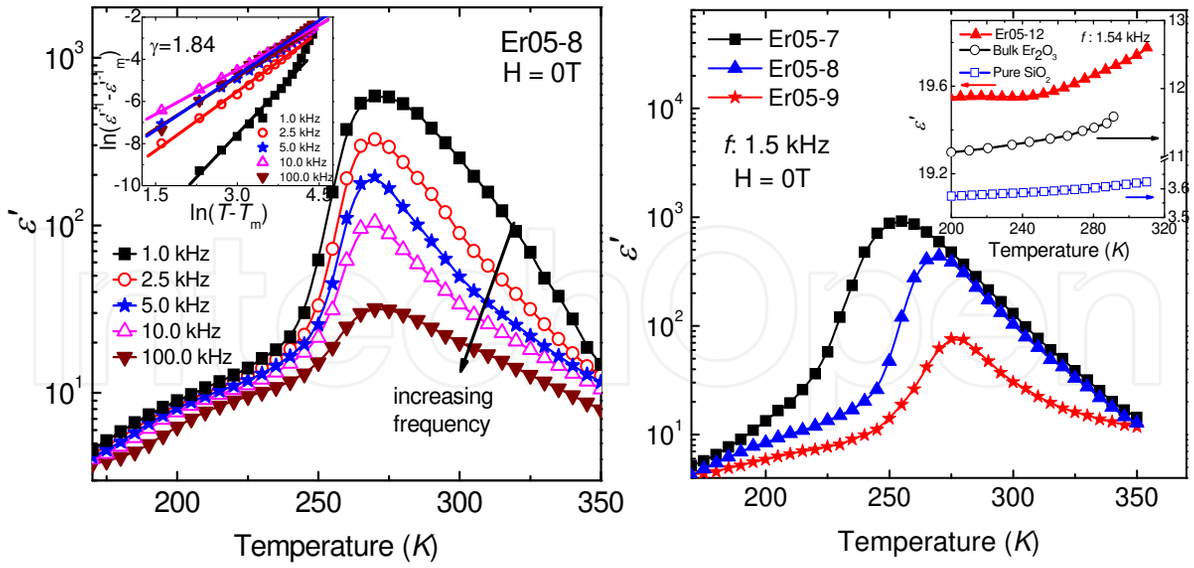

Figure 3. (Color online) (a) The (ε'-T) curves of Er05-8 at different selective frequencies, inset: representative plots of $\ln(\varepsilon'^{-1} - \varepsilon'^{-1}_m)$ vs. $\ln(T - T_m)$ of Er05-8 at temperatures > T_m, (b) (ε'-T) curves of Er_2O_3 nanoparticles dopes SiO_2 glass calcined at different temperatures, inset shows (ε'-T) curves of Er05-12 with respect to Bulk Er_2O_3 and SiO_2 showing non-DPT feature.

The plots of $\ln(\varepsilon'^{-1} - \varepsilon'^{-1}_m)$ vs. $\ln(T - T_m)$ at several frequencies are illustrated in inset of Figure 3(a). We obtained average $\gamma = 1.84$ from different slopes of linear fitting, which is close to the relaxor value like other oxide relaxor systems [30]. The enhancement of dielectric value is observed even at temperatures below T_m (~ 250–260 K), which ruled out the possibility of any space charge or interfacial polarization. The high dielectric value associated with DPT behavior (Figure 3(b)) diminishes with increasing calcined temperature (i.e., the Er_2O_3 NPs size). It is relevant to mention here that the temperature and frequency dependent dielectric phenomena of Er05-12 crystalline sample (calcined at 1200°C) without DPT behavior behaves like pure bulk Er_2O_3 [28] or SiO_2 glass (inset of Figure 3(b)). The critical calcination temperature above which DPT behavior completely diminishes for this typical concentration of Er_2O_3 (~ 0.5 mol %) is found to be around 1000°C. The DPT behavior is thus confined to the low temperature calcined (< 1000°C) system only where the NPs are in the 2–10 nm range.

4.2. Dielectric relaxation analysis

To shed more light on the relaxation dynamics of rare earth oxide NPs-glass composite systems, temperature dependent dielectric loss tangent (tanδ) are carried out at various frequencies. The appearance of three maxima with strong frequency dispersion located at peak *A* ~180 K, peak *B* ~ 260 K, and peak *C* > 320 K are observed in tanδ vs. temperature curve. The former two peaks (peaks *A* and *B*) are shifted to high temperature with increasing frequency, whereas, the peak *C* with high-dielectric leakage (~ 7) is shifted to the lower temperature. In Figure 4(b), the temperature dependence logarithmic plot of the relaxation time (τ), determined as the inverse of the maximum peak frequency exhibit straight line, is shown in an Arrhenius representation $\tau = \tau_o \exp(E_{relax}/kT)$, with an energy barrier E_{relax}. Near the DPT temperature (T_m), thermally

http://dx.doi.org/10.5772/60677

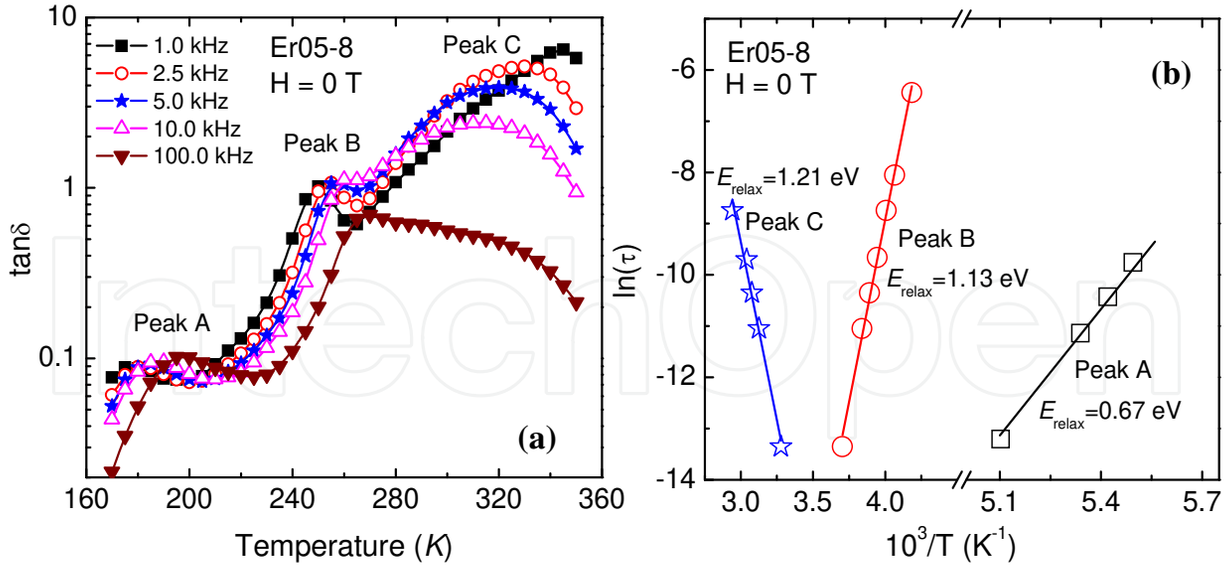

Figure 4. (Color online) (a) Dielectric loss tanδ of Er05-8 at different frequency, (b) representative Arrhenius plot of the relaxation time of Er05-8. The calculated activation energy values (in electron volt (eV)) are illustrated in each case.

activated response is described with an energy barrier E_{relax} of about 1.13 eV. However, the temperature dependent relaxation response above 300 K becomes reversed with the activation energy 1.21 eV. These experimental facts suggest the presence of thermally activated oxygen vacancies associated with the dielectric relaxation process as presented earlier with activation energy ~ 0.7-1.2 eV [30,31]. Our present results support the recent experimental finding of perovskite type ABO_3 [31] material, closely related to the thermally activated reorientation of dipole moment via the oxygen ion jumping through the oxygen vacancy, which can be controlled by sintering process. The dielectric response and DPT behavior diminishe by long-time annealing of the sample at higher temperature, which might be associated with reduced concentration of oxygen vacancies. Here, electrode effect in dielectric measurement is excluded by using different thickness of the samples with different electrode materials, indicating the intrinsic nature of this system.

4.3. Polarization studies

Figure 5 shows the frequency and temperature dependence hysteresis loop (*P-E* curves) of typical Er05-8. The values of remanent polarization (P_r ~ 0.032 μC/cm^2) and coercive field (E_c ~ 0.78 kV/cm) of relatively narrow *P-E* loop near T_m (~270 K) without saturation are attributed to noncanonical ferroelectric-like (FEL) correlation in the sample, similar to those commonly observed in ABO_3 perovskites [32]. However, the present NP-glass composite system has very high magnetic dilution of the NPs Er_2O_3 concentration (0.5 mol% Er_2O_3 : 99.5 mol% SiO_2) and hence small amount of dipole moment per unit volume are not high enough to induce significant changes in the polarization. The spurious hysteresis loop reveals some contribution of lossy dielectric (space charge such as oxygen vacancies) or nicknamed as "banana loops," the terminology recently coined by Scott [33]. At lower frequency, the hysteresis loop becomes slightly fatter. However, to check the possible FEL correlation in the sample, temperature

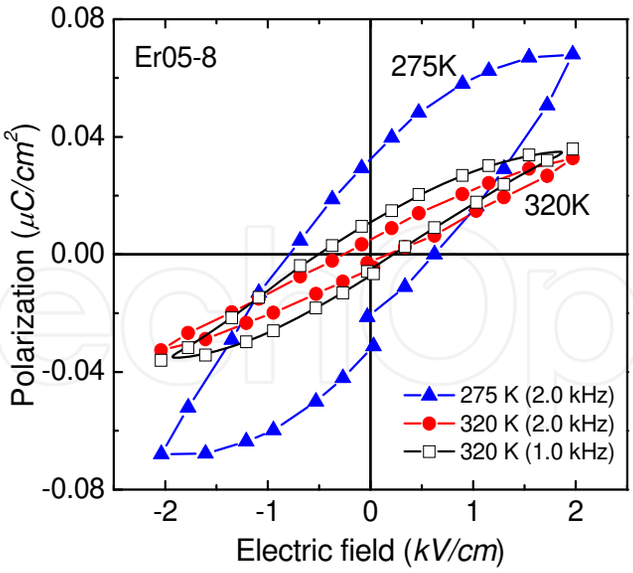

Figure 5. (Color online) Dielectric hysteresis loop of Er05-8, measured near DPT (275 K) and above room temperature (320 K) using 2.0 and 1.0 kHz polarization frequency.

dependent *P-E* characteristics are carried out at highest polarization frequency (2.0 kHz), obtained in our instrument (Precision LC meter, Radiant Technologies). It is noted that the measured hysteresis loop at high frequency is closely related with the intrinsic ferroelectric switching processes of the system [34]. Although, the values of remanent polarizaion and coercive field of *P-E* curves becoming more pronounced with decreasing temperature from 320 to 275 K suggesting ferroelectric-like ordering in NPs-glass composite system, further investigations are certainly needed to delineate it.

4.4. Equivalent circuit analysis

Materials exhibiting colossal enhancement of dielectric value are usually adopted to explain by Maxwell–Wagner (MW) mechanism. The present NPs-glass composite system is basically NPs grain of rare earth oxide (uniformly distributed) embedded in more insulating SiO_2 matrix. The enhancement of dielectric constant along with DPT behavior might be a signature of the effect of internal barrier layer capacitance depending on the ration of grain size and the grain-boundary thickness. The complex impedance curves in Figure 6 have also been analyzed using an equivalent circuit, consisting of the two inclined semicircular arc (deviation from the ideal Debye response). Thus, the two depressed semi-arc in the Nyquist plot (complex impedance Z″-Z′plane) of the impedance data could be modeled on two parallel resistor–capacitor (RC) networks connected in series, one corresponds to the conducting part in high frequency region assigned to the intrinsic effect of grain (typical Er_2O_3 NPs) and the other arc in low frequency side corresponds to the more resistive part (SiO_2 matrix) of the sample. Interestingly, the entire measured frequency region (20 – 2 × 10^6 Hz) at the temperature below T_m (<270 K) is governed by the grain response (intrinsic effect). The temperature dependence of grain (Er_2O_3) resistance (R_g) values are obtained from equivalent circuit model with the help of commercial software (Z-VIEW, version 2.9c). The contribution of grain resistance (intrinsic

http://dx.doi.org/10.5772/60677

response of NPs-glass systems) in the presence of magnetic field effect are discussed in the next section.

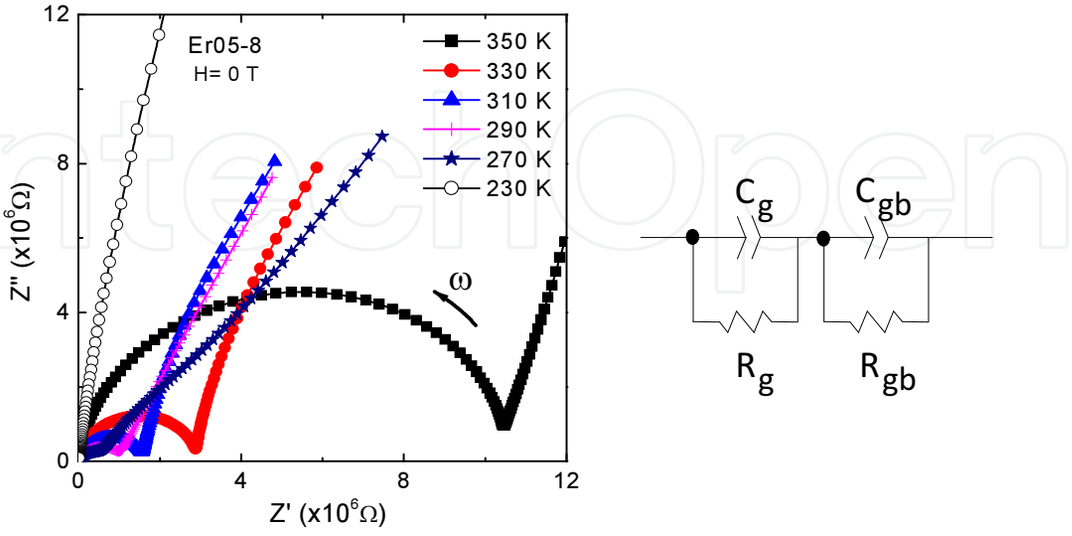

Figure 6. (Color online) (a) Complex plane plots, Z″-Z′, of Er05-8 at several temperatures and (b) schematic model of equivalent electrical circuits indicating of two parallel resistor–capacitor (RC) combinations [(R_gC_g): Er_2O_3 nano-grain, ($R_{gb}C_{gb}$): SiO_2 matrix] connected in series.

4.5. Magnetodielectric effect

The observation of colossal MD effect is the most interesting finding of Er05-8 system as shown in Figure 7(a) at a specific frequency of 2.5 kHz. The large enhancement of dielectric constant (~2.75 times) is observed around the transition regime 260–300 K under 9 T magnetic field. The inverse of dielectric constant with temperature under magnetic field (upper inset of Figure 7(a)) are also fitted by Curie–Weiss law with Curie constant (C) (3968.82, 6211.29 and 6918.04 K for 0, 5 and 9 T, respectively) and Curie–Weiss temperature (T_o) (260.06, 270.12 and 271.64 for 0, 5 and 9 T, respectively). It is obvious that both dielectric temperatures (T_m and T_o) are shifted to higher temperatures with increasing magnetic field, indicating the occurrence of magnetic spin-ordering at higher temperature under magnetic field and hence exhibit a reduced spin-lattice coupling strength under magnetic field. Temperature and frequency dependent dielectric constant of Er05-7 and Er05-8 are measured at a typical higher magnetic field (~9 T), shown in Figures 7(b) and 7(c). One may speculate about particle size dependent field effect playing a role of the larger ε′ response in the lower temperature annealed samples [35]. Within this scenario, the system in which we observed MD effect as well as Curie–Weiss behavior is the single phase of amorphous Er_2O_3 NPs of 2–10 nm size embedded in SiO_2 glass calcined at 700–900°C. The estimated field dependent MD response (MDR) near T_m (~275 K) is defined by $\{\Delta\varepsilon'(H)/\varepsilon'(0)\% = [[\varepsilon'(H)-\varepsilon'(0)]/\varepsilon'(0)]\times 100\}$ as a function of the square of the magnetization as shown in the lower inset of Figure 7(a). Strikingly, the fractional change of the magnetic field induced change in the dielectric constant can be well approximated by the scaling function, $\Delta\varepsilon'/\varepsilon' \approx \alpha M^2$, where magnetoelectric interaction constant, α is estimated at 0.782.

Similar behavior of the change in dielectric constant on the square of the magnetization is also observed in several materials including intrinsic multiferroics, such as $BiMnO_3$ [36], suggesting MD response in the present system (magnetic NPs of the guest oxide and SiO_2 host glass) are closely related to the magnetism, typical size and concentration of the Er_2O_3 NPs.

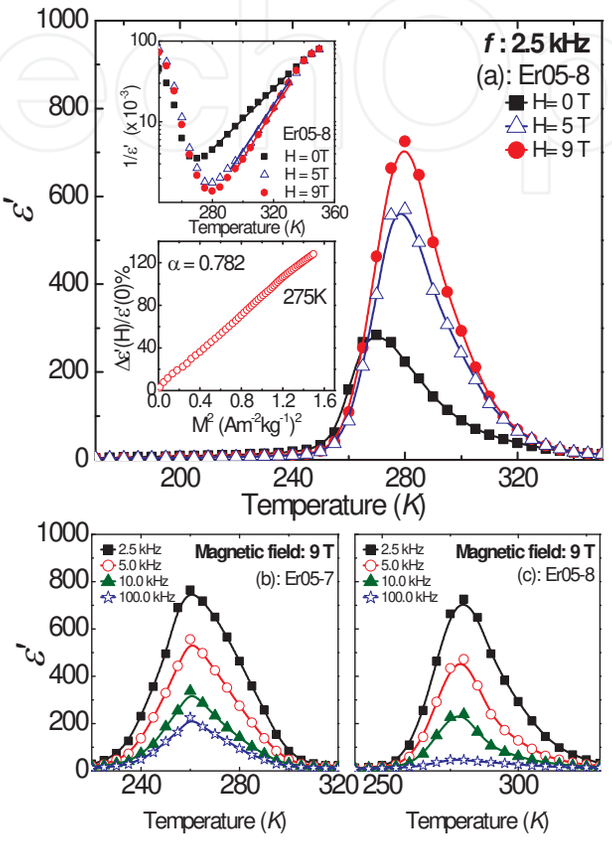

Figure 7. (Color online) (a) The magnetic field dependence of (ε'-T) curves of Er05-8 at a fixed frequency 2.5 kHz. Upper inset of (a): inverse of ε' with temperature under magnetic field exhibiting the Curie–Weiss behavior and the lower inset of (a): the fractional change of the magnetic field induced change in the dielectric constant ($\Delta\varepsilon'/\varepsilon'$) of Er05-8 showing linear variation with the square of magnetization M^2, measured in the vicinity of T_m (~ 275K). [(b), (c)] (ε'-T) curves of Er05-7 and Er05-8 samples measured with several selective frequencies under 9 T applied magnetic field.

4.6. Micro-structural correlated resistivity analysis

Figure 8 shows the contribution of amorphous NP Er_2O_3 grain resistance R_g (calculated from equivalent circuit element analysis in Figure 6) of Er05-8 under external magnetic field as a function of measuring temperature. The temperature dependence of *ac* conductivity (σ_{ac}) at various frequencies is demonstrated in Figure 9. In the inset of Figure 9, the *ac* conductivity as a function of temperature under external magnetic field is illustrated. Concomitantly, the grain resistance $R_g(T)$ in Figure 8 exhibits a metal to insulator like transition coinciding with the dielectric maxima temperature T_m of $\varepsilon'(T)$ (Figure 3(a)) as well as $\sigma_{ac}(T)$ (Figure 9). Interestingly, the R_g decreases under magnetic field, similarly observed in colossal magnetoresistive

http://dx.doi.org/10.5772/60677

materials [25]. These experimental facts truely corroborate that the nature of charge carriers responsible for *dc* conduction in the grain interior and the dielectric relaxation maxima belongs to the same category.

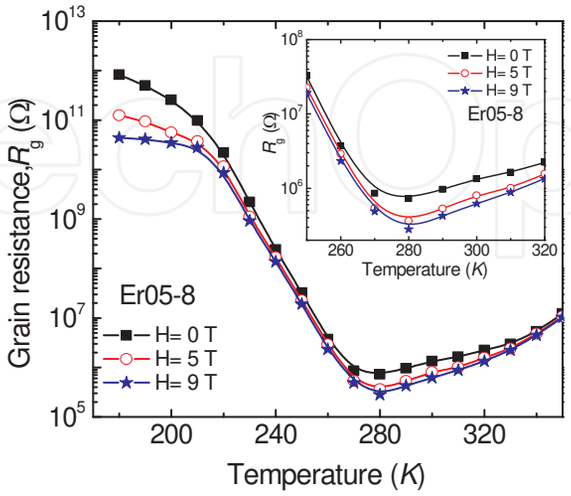

Figure 8. Color online) Temperature dependence of grain resistance (R_g) calculated from impedance complex plane plots with external magnetic field. Inset: The region close to T_m is highlighted.

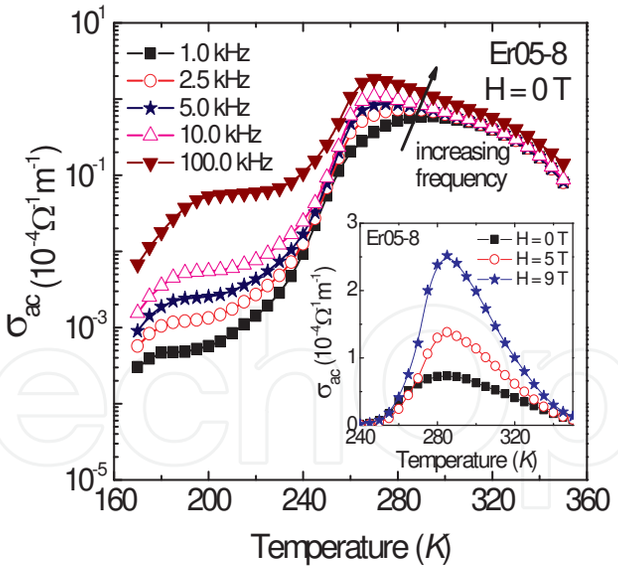

Figure 9. (Color online) Temperature dependence of *ac* conductivity (σ_{ac}) of Er05-8 for various frequencies. Inset: temperature dependence of *ac* conductivity (σ_{ac}) at 2.5 kHz with external magnetic fields.

The magnetoresistive property of magnetic NPs is attributed by spin-polarized tunneling [37]. Although, the observed strong positive magnetoelectric interaction constant (α~ 0.782) has a similar appearance to intrinsic multiferroics, the MD effect can also be achieved through a combination of magnetoresistance and the Maxwell–Wagner effect, as predicted by Catalan

[38]. Since the current results suggest that MD behavior is probably a manifestation of magnetoresistance changes, depending on the NP size and separation. Enhancement of MD response (i.e., positive MD effect) through the decreases of NPs Er_2O_3 resistance under external magnetic field, (i.e., negative magnetoresistance) might imply the possible tunability of the resistive MD effect.

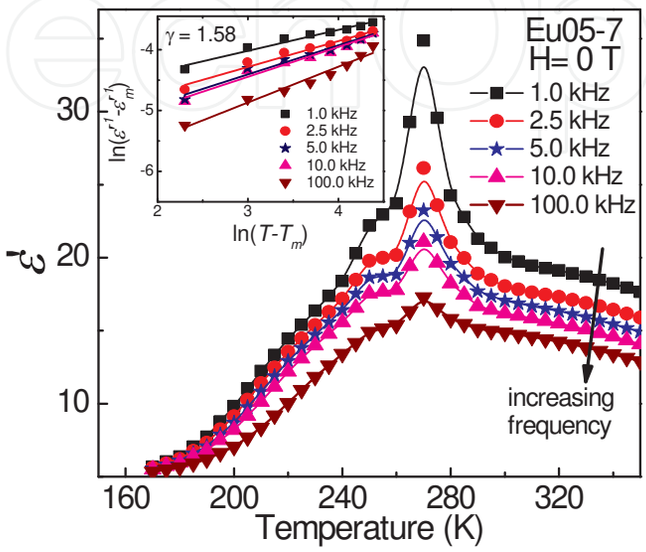

Figure 10. (Color online) (a) The (ε'-T) curves of Eu05-8 at different frequency, inset: representative plots of $\ln(\varepsilon'^{-1} - \varepsilon'^{-1}_m)$ vs $\ln(T - T_m)$ at temperatures higher than T_m for the Eu05-8 at different frequency values.

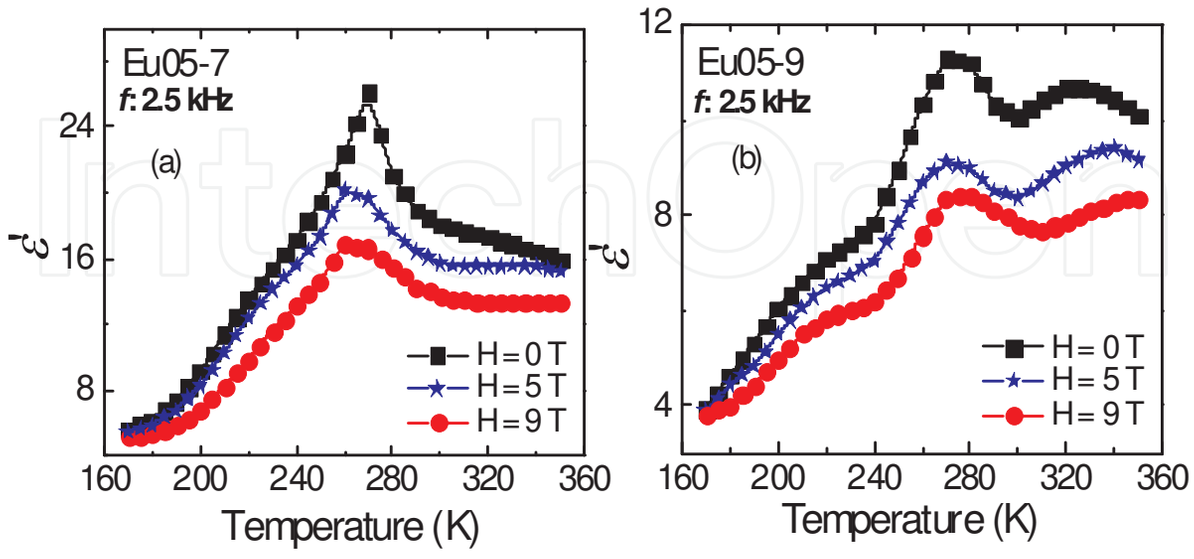

Figure 11. (Color online) (a), (b) The (ε'-T) curves of Eu05-7 and Eu05-9 measured under different applied magnetic fields at a fixed frequency 2.5 kHz.

http://dx.doi.org/10.5772/60677

5. Eu_2O_3 NPs-glass composite system: Smaller dielectric response and negative MD effect

Typical data is shown for Eu_2O_3:SiO_2 NPs-glass composite system having 0.5 mol% dopant Eu_2O_3 concentration calcined at different temperatures, namely, 700, 800 and 900°C (henceforth referred as Eu05-7, Eu05-8 and Eu05-9 respectively). Figure 10 represents the temperature dependence of $\varepsilon'$of Eu05-7 in the absence of the magnetic field. The nature of the variation of the (ε'-T) curves with maxima at $T_m \sim 270$ K, represents as "diffuse phase transition" (DPT) around T_m with smaller ε' than Er05-7 system, quite different and larger than that of bulk Eu_2O_3 [28] or pure SiO_2 (~ 3.9). Such system also follows a modified Curie–Weiss relationship [29], obtaining diffuseness exponent γ =1.58 (inset of Figure 10). The ε'-T plot (at 2.5 kHz), around the transition regime 240-320 K of Eu05-7 and Eu05-9 shows a decrease of ε' under a magnetic field of 9 T (Figure 11). Here, we also observed particle size dependent effect, associated with DPT behavior as well as MD effect.

6. Effect of different rare earth oxides on the dielectric properties

In previous sections, we have presented interesting particle size dependent colossal dielectric response along with MD effect in Er_2O_3 and Eu_2O_3 nano-glass composite systems. From the obtained results, there are colossal enhancement of dielectric constant and large MD effect in Er_2O_3 case [20], while those in Eu_2O_3 case, smaller responses were observed [39]. Obviously, the different electronic and magnetic properties for Er_2O_3 and Eu_2O_3 play a crucial role. However, these results suggest great promise in further systematic investigation to distinguish the mechanisms that contribute to colossal dielectric responses along with MD effect in other RE_2O_3:SiO_2 nano-glass composite systems (RE_2O_3, RE ~ rare earth, a series of elements from La to Lu with stable RE^{3+}) with different RE_2O_3 NPs size.The purpose of such study is to find amorphous high-k oxide candidates and MD effect with superior phase stability for gate dielectrics from a lineup of rare earth metal oxides embedded in SiO_2 matrix, and to find a sequential coupling between different constituents among these nano-glass composite materials.

Figure 12 illustrates the temperature dependent ε' of the series of rare earth oxide NPs-glass composite systems calcined at 700°C in the absence of the magnetic field. Here, we concentrate the variations of temperature dependent dielectric behavior mainly on the 700°C calcined sample for the sake of clarity. Besides that, the possibility of formation of other rare earth oxide phase (e.g., $RE_2Si_2O_7$) mixture with crystalline RE_2O_3 is ruled out at 700°C for low dopant concentration (0.5 mol%) [22]. Interestingly, RE_2O_3:SiO_2 nano-glass composite systems in which RE ~ Sm, Gd and Er show colossal enhancement of dielectric constant ($\varepsilon' \sim 10^3$) around room temperature. The nature of the variation of the (ε'-T) curves represents well-defined maxima and notable dielectric broadening around ε'_m (maximum value of ε') with high ε' and different from pure bulk RE_2O_3.

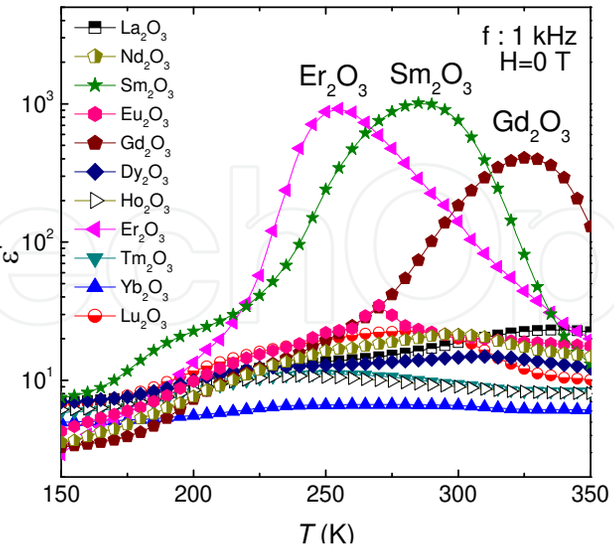

Figure 12. (Color online) The ε'-T curves of RE_2O_3 (gel-glass calcined at 700°C) at 1 kHz without applied magnetic field.

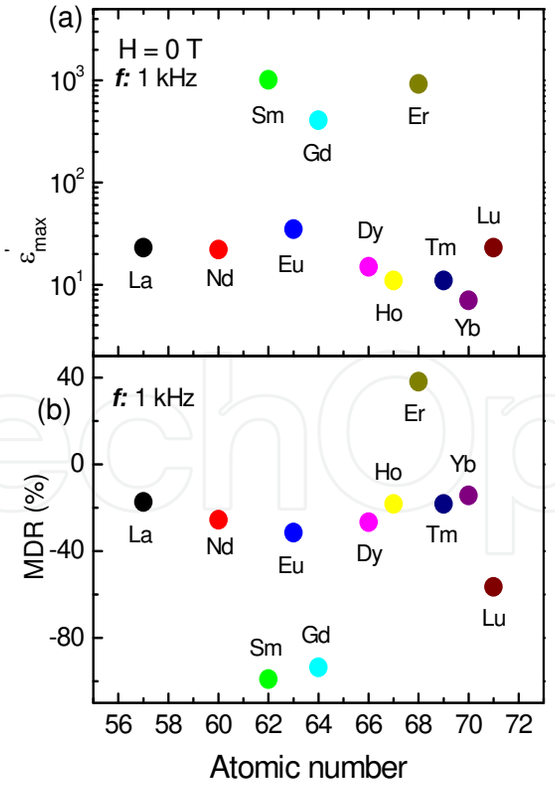

Figure 13. (Color online) (a) Maximum value of dielectric constant, and (b) MDR under 5 T applied field of RE_2O_3:SiO_2 nano-glass composite systems calcined at 700°C with rare earth atomic number.

http://dx.doi.org/10.5772/60677

The amorphous self-organized rare earth oxide nano-glass composite systems may be the promising high-*k* gate dielectrics due to its reproducible high dielectric constant (Figure 13(a)), single-stage process in air at moderate temperature and good compatibility with modern microelectronics processing technique. The present systems also show the MD effect around the transition temperature. The MDR at 1 kHz is plotted as a function of atomic number of the rare earth elements near T_m as shown in the Figure 13(b). The RE_2O_3:SiO_2nano-glass composite systems in which RE ~ Sm, Gd, Er and Lu show colossal response of dielectric constant under applied magnetic field. Sol–gel process provides a convenient way for tailoring phase pure, self-organized NPs of nearly uniform sizes (particle size distribution histogram from TEM image) and for facilitating homogeneous dispersion of these metal-oxide NPs in the silica matrix. It is believed that the sol–gel derived NP-glass composite systems prepared and calcined in identical condition (Figure 1(b)), the particle size distributions of all rare earth oxide at specific calcined temperature is nearly equal (say 700°C, we have checked for Er, Eu, Gd and La systems). These rare earth oxide NPs are rigidly fixed within the insulating silica matrix at all temperatures. So this dielectric behavior does not arise from the physical motion of the NPs. This feature takes place inside the rare earth NPs grain and they are very much conditioned by magnetic property of NPs grain, the potential barriers in the grain boundaries, the degree of deformation of the lattice and the crystallites, as well as the grain size and their constituent host. Why RE ~ Sm, Gd and Er shows much larger effects than other rare earths? It needs further investigation using magnetic and non-magnetic rare earth oxide NPs together with different doping concentrations to explore the mechanism and application feasibility on these rich dielectric materials.

7. Effect of molar concentration of magnetic NPs on the observed dielectric and MD properties

As discussed in the above section, we have systematically investigated the colossal responses of dielectric behavior along with MD effect in rare earth oxide (RE_2O_3, RE ~ rare earth, a series of elements from La to Lu with stable RE^{3+}) NPs embedded SiO_2 glass composite systems with different RE_2O_3 NPs size. Properly annealed NPs-glass composites, where RE ~ Sm, Gd and Er, show an intriguing colossal response of dielectric behavior and MD effect near room temperature. These reproducible experimental facts suggest simultaneously a question why only these three magnetic rare earth elements have larger effects than others. Herein, we have systematically synthesized together via sol–gel route the magnetic Gd_2O_3 and non-magnetic La_2O_3 NPs with different doping concentrations and size embedded in SiO_2 matrix. The doping concentration and the corresponding sample index are highlighted in Table II [40]. Here, we report that the high-*k* and MD of these NP-glass composite systems are very much conditional by magnetic property of Gd_2O_3 NPs size, concentration, and the degree of deformation of the host matrix. To improve the dielectric tunability in presence of external magnetic field, the crucial magnetic properties of dielectrics are necessary for the application of the devices.

Sample name	Non-magnetic La_2O_3 (mol%)	Magnetic Gd_2O_3 (mol%)
LGS1	0.150	0.000
LGS2	0.120	0.030
LGS3	0.090	0.060
LGS4	0.075	0.075
LGS5	0.060	0.090
LGS6	0.000	0.150
LGS7	0.000	0.500

Table 2. Different doping concentrations of non-magnetic La_2O_3 and magnetic Gd_2O_3 (mol%) in SiO_2 NP-glass composite systems.

Figure 14 illustrated the ε'-T curves of La_2O_3/Gd_2O_3 NPs embedded SiO_2 glass composite systems (henceforth referred to as LGS) with different doping concentrations in the absence of the magnetic field. All the curves have well-defined diffuse phase transition-like maxima at T_m ~320 K characteristic with oxygen vacancy-induced dielectric relaxation, thoroughly discussed in our previously reported sections [16,20,39] of other rare earth systems. Interestingly, at higher magnetic Gd_2O_3 doping concentrations, the LGS NP-glass composite systems show colossal enhancement of dielectric behavior near room temperature. Even, a very high magnetic dilution of Gd_2O_3 NPs (LGS2 sample ~ doping level 0.03 mol%) system, the dielectric value is higher than that of pure bulk crystalline counterpart [28].

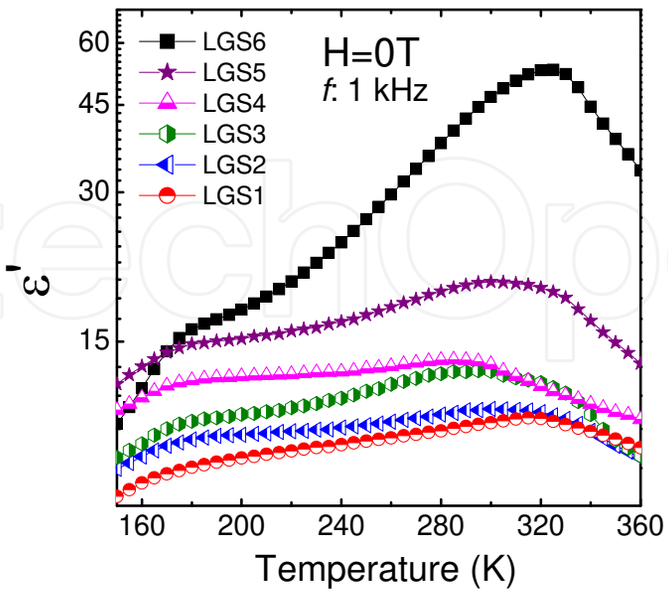

Figure 14. (Color online) The ε'-T curves of LGS NP-glass composite systems with different doping concentrations calcined at 700°C.

http://dx.doi.org/10.5772/60677

Figure 15(a) illustrates the ε'_{max} vs. Gd_2O_3 doping concentrations of NP-glass composite systems calcined at 700°C in the absence of the magnetic field. Here, ε'_{max} increases with higher doping concentration of magnetic Gd_2O_3 NPs. The present systems also show strong MDR around the transition temperature (T_m). The MDR at several selective frequencies near T_m are plotted as a function of doping concentration of Gd_2O_3, shown in the Figure 15(b). MDR enhances with faster rate at relatively lower doping concentration (≤0.1 mol%) of magnetic Gd_2O_3, whereas at moderate concentration range (≥0.2 mol%), the colossal response are more pronounced. A profound analogy may be expected between the colossal MDR in magnetic NP-glass composite systems and the inhomogeneous magnetoelectric interaction, inducing through magnetic spin modulation (flexomagnetoelectric polarization) [41]. Depending on the characteristic size (particle radius) and magnetization in amorphous-like nanosized systems, the flexomagnetoelectric effect induces linear magnetoelectric tunability [42].

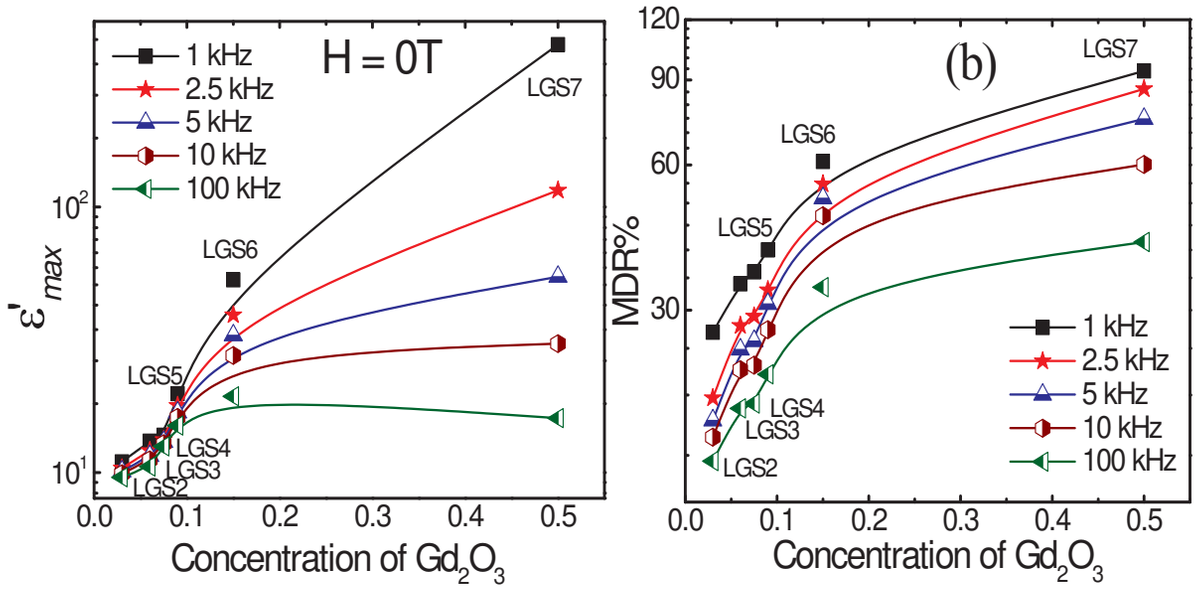

Figure 15. (Color online) (a) Maximum value of dielectric constant, and (b). MDR under 5 T applied field of LGS NP-glass composite systems with different Gd_2O_3 doping concentrations calcined at 700°C.

8. Extended X-ray Absorption Fine Structure (EXAFS) experiments

Extended X-ray absorption fine structure (EXAFS) experiments were performed at the Gd L_{III} edge to obtain further detailed information on the local surroundings of the chemical elements of the Gd-oxide doped (0.5 mol%) nano-glass composite system calcined at different temperatures, namely, 700, 800, 900, and 1200°C (henceforth referred as Gd05-7, Gd05-8, Gd05-9, and Gd05-12, respectively). The broad dielectric anomaly in Gd_2O_3:SiO_2 can be plausibly attributed to oxygen vacancy defects, which are implied by the EXAFS measurements. Of particular interest are the coordination number of oxygen around the Gd atom and type of neighbors,

the interatomic distance between the Gd atom and the surrounding oxygen, and the Debye–Waller factors which contain the mean-square relative displacements due to static disorder or thermal vibration. Figure 16 depicts the room temperature experimental EXAFS spectra of samples Gd05-7, Gd05-8 and Gd05-9. The EXAFS signals weighted by k^2 [i.e., $k^2\chi(k)$] are shown in Figure 16(a), and the moduli of their Fourier transforms $|F(R)|$ are presented in Figure 16(b). The EXAFS spectra in Figure 16(a) look very much the same, on the first glance, and thus one would not expect a major difference in the Fourier transform data. The Fourier transform modulus (Figure 16(b)) exhibits two main coordination peaks: the first one, located at R ~ 1.8 Å corresponds to the interatomic distances of Gd^{3+}–O (first coordination shell), while the second one (not growing properly) is located at R ~ 2.8 Å, indicating mostly the amorphous environment of Gd [21], as expected for a Gd–Gd coordination (second coordination shell) in a crystal. However, the TEM results confirm the presence of NPs Gd_2O_3 with localized crystallinity in the glass specimen calcined at 700°C. The fitting results of Gd^{3+}–O interatomic distances obtained from Figure 16 are summarized as a function of calcination temperatures in Table III. The values obtained from the EXAFS spectra are not significantly different in all the glass specimens with very low doping concentration. However, on close inspection it is evident that the average Gd^{3+}–O interatomic distance of Gd05-7 is shorter than that of Gd05-8, Gd05-9, and bulk Gd_2O_3 (unsupported SiO_2 glass matrix), suggesting that oxygen ions surrounding the oxygen vacancies around Gd ions should concurrently involve a relaxation toward their adjacent vacancies and, as a result, shorter bond length can be attributed [43]. This argument can, presumably, also be applied to the Er_2O_3:SiO_2 NP-glass system. It has been found that the porous glass are formed at ~ 400°C and annihilation of pores start at ~ 700°C, completed at ~ 800°C [44]. Therefore, silica gel-glass doped with low concentration of rare earth ions are subjected to systematic heating, the collapse of the silica pores is initiated near 700°C (Si–OH groups condense to Si–O–Si bonds). In this calcined glass, agglomeration of individual rare earth oxide ions loosely attached to the pores to be detached to form clusters. The dimensions of the clusters reside in the nanometer range. At 700°C calcined sample, in rare earth oxide NPs, oxygen vacancies could be easily created by loss of oxygen at low oxygen partial pressure, according to $O_0 \leftrightarrow V_0 + 1/2O_2$. Based on these considerations, the formation of oxygen vacancies inside the NPs influence the bond-length change, and the number of oxygen atoms surrounding the Gd atom should also decrease. This argument is in fair agreement with the result of a relative decrease in the number of nearest neighbors (Table III) in Gd05-7 in comparison with other high temperature calcined samples. At higher temperature, namely, 800°C, collapse of larger pores also takes place, agglomerate more RE_2O_3 to form bigger size NPs [18]. This implies that annealing at higher temperatures increase the particle size with lower V_0 concentration. These results are consistent with dielectric studies, resulting in the decrease in dielectric constant along with DPT behavior by annealing the sample at higher temperatures. Likewise, the Debye-Waller factor increases with decreasing NPs size, indicating that the disorder in oxygen environment increases with lower calcination temperatures. In this connection, it is relevant to refer to the important findings of RE^{3+} doped EXAFS studies by Rocca *et al*. [45] on the densification of silica xerogels as a function of heat treatment up to 900°C. Their measurements have shown that the densification of xerogel without evidence of clustering of RE^{3+} induces a decreasing of the co-ordination number and a shortening of the

http://dx.doi.org/10.5772/60677

main RE–O distance and absence of RE–RE correlation. Nevertheless, our TEM studies in densified glass specimens (700°C and above) have revealed clear detectable NPs with separation. So, it is reasonable to assume that the shortening of Gd^{3+}–O and the decreasing of the coordination number with lower calcined nano-glass specimens depends on NPs size (or, more correctly, the oxygen vacancy) for which further experiments of all the rare earth with different doping concentrations are still necessary. Therefore, our EXAFS findings provide additional insight into the origin of the unusually colossal room-temperature dielectric response in rare earth oxide NPs embedded oxide glasses.

Sample	Bond type	EXAFS		
		N	*R+Δ (Å)*	σ^2 *(Å²)*
Gd05-7	First coordination shell (Gd^{3+}–O)	5.3±0.2	2.216±0.012	0.016±0.002
Gd05-8		5.6±0.2	2.234±0.011	0.015±0.003
Gd05-9		5.8±0.3	2.248±0.013	0.014±0.002
Gd_2O_3		6.0±0.2	2.265±0.012	0.007±0.003

Table 3. Results of the quantitative analysis of the first coordination shell derived from EXAFS filtered data of Gd_2O_3:SiO_2 nano-glass composite systems at different calcinations temperatures. *N*, *R* and σ^2 are the average coordination number, interatomic distance, and relative mean square displacement (Debye-Waller factor), respectively.

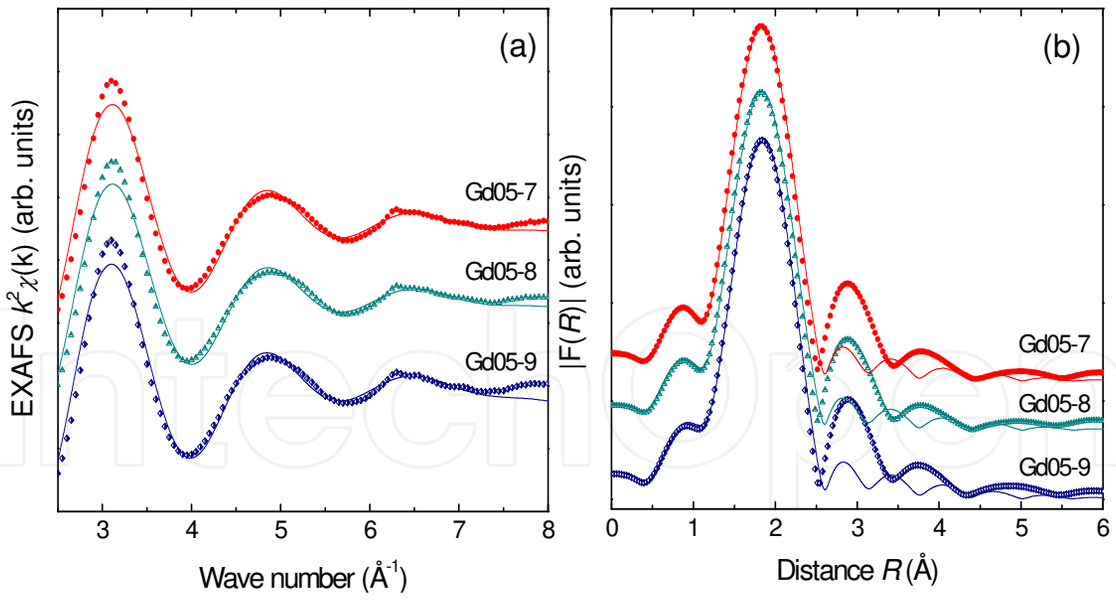

Figure 16. (Color online) Gd L_{III}-edge EXAFS spectra of Gd^{3+}-doped SiO_2 glass samples calcined at different temperatures. Spectra are vertically shifted for clarity. (a) k^2-weighted EXAFS signals. (b) Fourier transforms moduli radial distribution functions. Both experimental data (symbols) and the best-fit theoretical curves (dashed) are also reported. The transformation range is k = 2.5–8 Å^{-1} for all the spectra and the range for the first coordination shell fit is R = 1–3 Å.

Figure 17 depicts the room temperature experimental EXAFS spectra of LGS systems ((La, $Gd)_2O_3$:SiO_2 NP-glass composite systems) with different doping concentrations (Table II) and

particles size (different calcined temperatures). The first coordination peak located at ~1.8 Å (Figures 17(a), (b)) with the interatomic distance of La^{3+}-O/Gd^{3+}-O looks very much the similar without any perceptible shift at different doping concentrations. However, the interatomic distances of the first coordination peak (~1.8 Å) of LGS4 with different calcination temperatures (Figures 17(c), (d)) are shifted significantly even with very low doping concentration of La_2O_3/Gd_2O_3. It reveals significantly that the average La^{3+}–O/Gd^{3+}–O interatomic distances of LGS4 samples at lower calcination temperature is shorter, suggesting higher oxygen vacancies around La/Gd ions, supported with our previously reported article [16]. Therefore, the dielectric value decreases by annealing the sample at higher temperatures (or, more correctly, with higher NPs size) with identical molar concentration of dopant element. However, identical particle size (magnetic and/or non-magnetic NPs) with concentration dependence does not affect the oxygen vacancies. In other words, oxygen vacancies depend only on the particle size but not its magnetic phase.

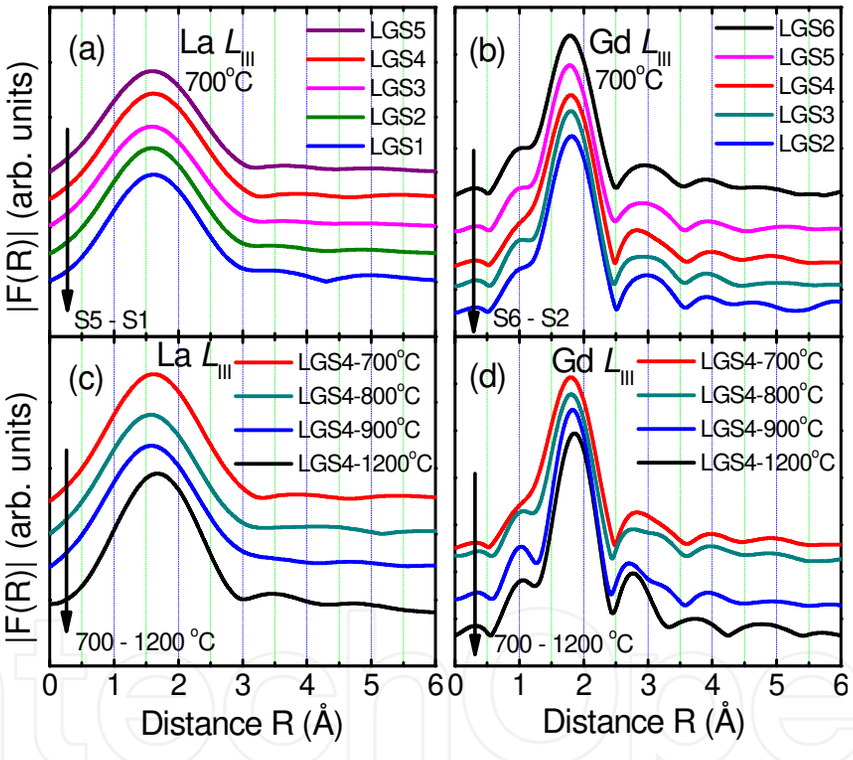

Figure 17. (Color online) Room temperature Fourier transforms moduli radial distribution functions EXAFS spectra of LGS systems at (a) La L_{III}-edge with different La_2O_3 concentrations, (b) Gd L_{III}-edge with different Gd_2O_3 concentrations calcined at 700°C, (c) La L_{III}-edge of LGS4 sample at different calcined temperatures, and (d) Gd L_{III}-edge of LGS4 sample at different calcined temperatures. Spectra are vertically shifted for clarity.

9. Magnetic measurements

The *dc* magnetization (after diamagnetic correction) of LGS5 sample under zero-field-cooled (ZFC) and field-cooled (FC) condition as a function of temperature (2–350 K temperature

http://dx.doi.org/10.5772/60677

range) in the presence of an applied magnetic field of 200 Oe are shown in Figure 18. It is noteworthy that the observed temperature dependent magnetic feature of LGS5 sample is attributed from magnetic transition of Gd_2O_3 NPs only. On close inspection, the divergent behavior between ZFC and FC data occurs at low temperatures (irreversibility temperature, T_{irr}) with a rounded maximum for ZFC curve is obtained at 58 K (identified as the blocking temperature, T_B). A spread in the blocking temperature may be rightly assumed with NPs size distribution. Such behavior is akin to superparamagnetic phase of Gd_2O_3 NPs in the nano-glass composite system similarly observed in oxide glasses containing Gd_2O_3 [46]. This typical characteristic temperature would be unlikely arising from a magnetic transition in oxygen contaminant [47]. The FC magnetization increases continuously with the lowering of temperature below the irreversibility temperature, consistent with ferromagnetic-like ordering of Gd_2O_3 NPs. The shape of the inverse susceptibility data (right axis of Figure 18) reveal a quite different behavior in comparison with usually found Curie-type behavior in bulk Gd_2O_3 [48].

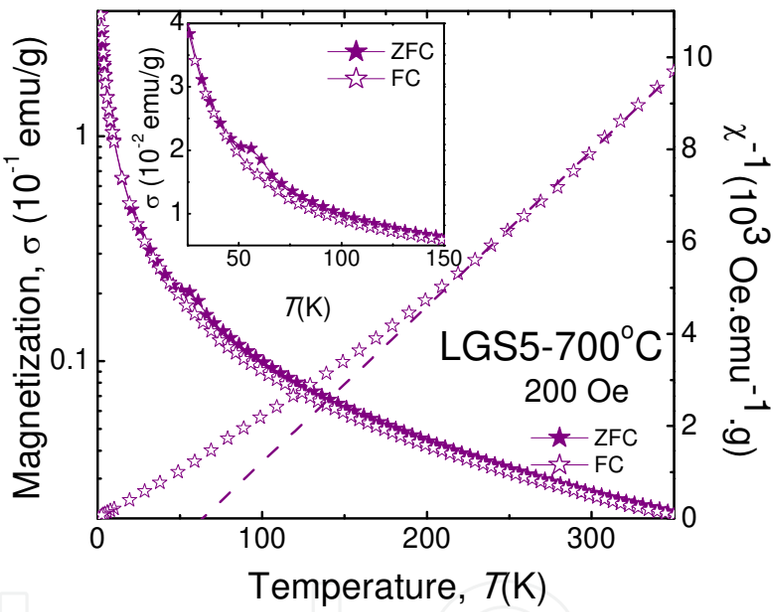

Figure 18. (Color online) ZFC and FC magnetization versus temperature curves of LGS5 sample calcined at 700°C, right axis shows the temperature dependent inverse susceptibility curve. In the inset, the region close to the superparamagnetic transition is highlighted.

The data obtained for the temperature dependence magnetization of LGS4 samples calcined at 700, 800, 900 and 1200°C are graphically depicted in Figure 19. The superparamagnetic blocking temperature cannot be traced in low accuracy (or resolution) of measurement with very low percentage-doping (~ 0.075 mol%) of magnetic Gd_2O_3. However, from the observed continuous increase in ZFC and FC curves at low temperature indicating the ferromagnetic nature of the LGS4 sample. Magnetic properties with size dependency are also observed for LGS4 samples calcined at different temperatures, related with the uncompensated surface spins present on the Gd_2O_3 NPs. It is likely that the Gd_2O_3 NPs with smaller size (i.e., higher surface-to-volume ratio) contain larger proportion of uncompensated surface spins and

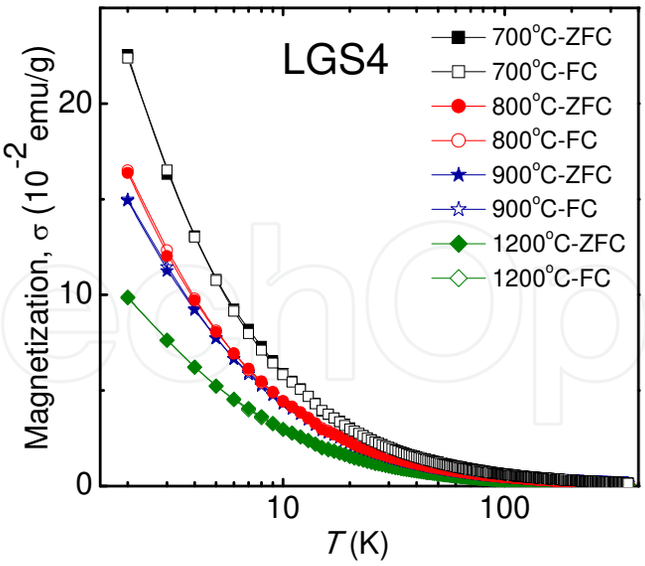

Figure 19. (Color online) ZFC and FC magnetization versus temperature curves of LGS4 sample at different calcination temperatures. Applied *dc* magnetic field 200 Oe.

consequently reveal higher ferromagnetic values than larger NPs (higher calcined temperature). Temperature dependent inverse susceptibility data for LGS4 samples calcined at different temperatures with respect to bulk Gd_2O_3 can be fitted by the Curie–Weiss law (Figure 20(a)) having different slopes of straight lines. The intersection points of fitted lines with *x*-axis exhibit the Curie–Weiss temperatures, found to be 32.7, 16.6, 12.1 and 4.8 K for 700, 800, 900 and 1200°C respectively. These positive values for LGS4 sample calcined at different temperatures indicate weak ferromagnetic behavior, whereas, bulk Gd_2O_3 shows antiferromagnetism with negative Curie–Weiss temperature at -16.3 K. The current tendency of lowering Curie-Weiss temperatures with increasing calcined temperature for LGS4 samples infers that lager sized Gd_2O_3 NPs possess toward bulk crystalline counterpart.

Isothermal magnetization-field sweeps were performed to further investigate the nature of the superparamagnetic state and the ferromagnetism below transition temperature. Figure 21 displays the magnetic field dependence of the magnetization (*M-H*) curves for LGS4 sample calcined at 700°C at 300, 200, 100 and 5 K in the *dc* magnetic field range ±60 kOe. Defining the magnetic characteristics, magnetic hysteresis curve obtained at 300 K has zero area, whereas, there is a dramatic change both in magnitude (enhancement of magnetic moment/unit mass) and shape (deviate from linearity) with measurable finite areas at 5 K (lower inset of Figure 21). This constitutes strong evidence that at 5 K the Gd_2O_3 NPs are going to the magnetically ordered state or in ferromagnetic nature. Moreover, magnetization vs *H*/*T* curves plotted at different temperatures are linear and collapse to a single curve (upper inset of Figure 21) confirming the existence of superparamagnetic phase of Gd_2O_3 NPs embedded in SiO_2 glass matrix. It is abundantly clear that Gd_2O_3 NPs grown with high magnetic dilution in glass matrix are best described as an assembly of non-interacting superparamagnetic NPs. The hysteresis curves have no magnetic saturation in the magnetic field range of ±60 kOe, considering large anisotropic fields appears in the Gd_2O_3 NPs systems [49].

http://dx.doi.org/10.5772/60677

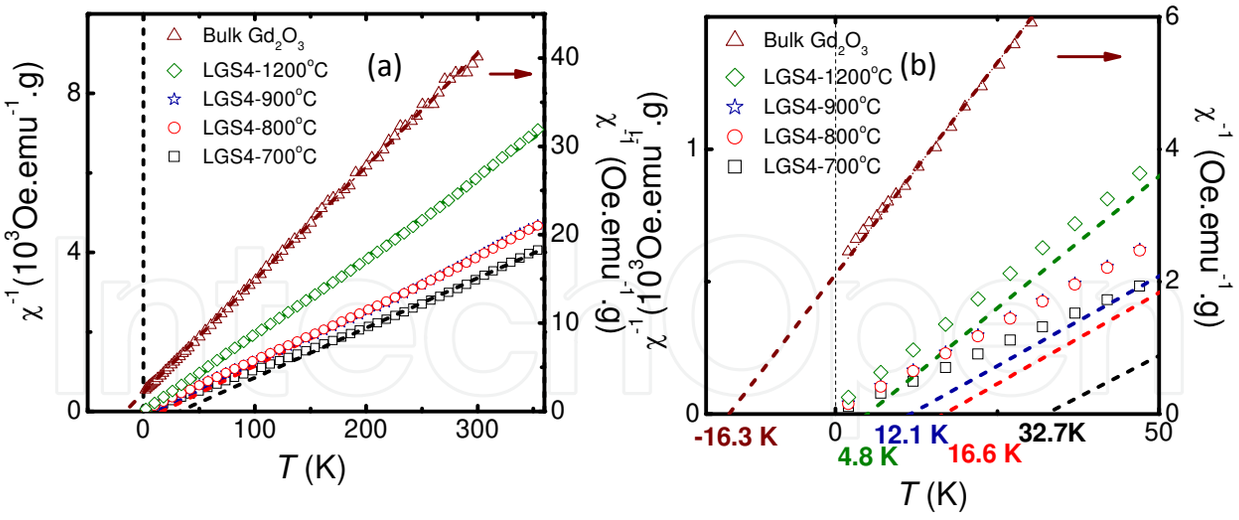

Figure 20. (Color online) (a) Inverse susceptibility versus temperature curves of LGS4 samples at different calcination temperatures with respect to bulk Gd_2O_3, (b) the region close to the extrapolated lines intersect with temperature axis is highlighted.

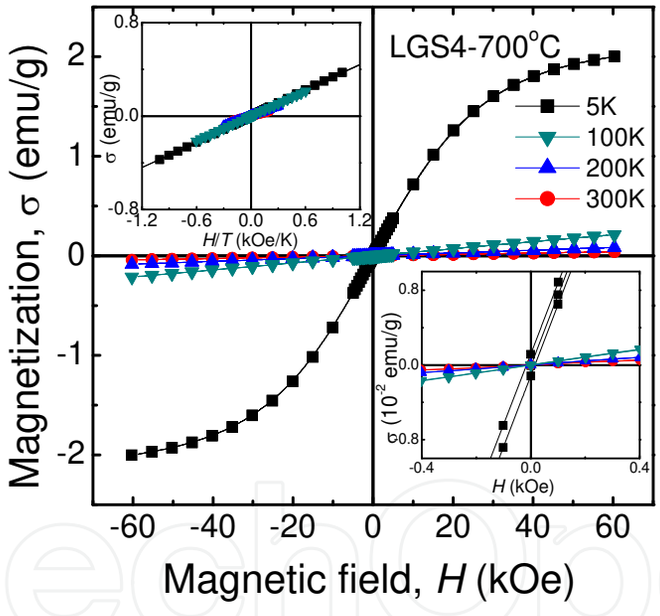

Figure 21. (Color online) Hysteresis loop of LGS4 sample calcined at 700°C, lower inset: the region close to the coercive field value is highlighted, upper inset: magnetization vs. H/T of LGS4 sample.

10. Conclusions

We have synthesized self-organized RE_2O_3 NPs with almost equal size and separation embedded in SiO_2 glass matrix by the sol–gel method.

Principal findings may be summarized below:

a. Presence of superparamagnetic phase occurs in magnetic rare earth oxide NPs doped glass samples.

b. Properly annealed sol–gel glass (in which RE ~ Sm, Gd and Er) (Fig. 2) shows an interesting colossal response of dielectric constant along with DPT and MD behavior around room temperature.

c. The experimental facts strongly suggest that the dielectric anomaly with DPT behavior is related to oxygen vacancy-induced dielectric relaxation in the material without ferroelectric phase transition.

d. The MDR observed in this glassy composite is considered to be associated with the direct consequence of magnetoresistance changes depending on the calcination temperatures (magnetic NPs size).

e. However, keeping the NPs size constant, the increase in dielectric constant and MDR strongly depends on the magnetic property (superparamagnetism) of the rare earth ions.

Acknowledgements

This research was partially supported by the Ministry of Science and Technology, Taiwan under Grant No. NSC 103-2112-M-110-010-MY3.

Author details

S. Mukherjee[1,2], T. H. Kao[1], H. C. Wu[1], K. Devi Chandrasekhar[1] and H. D. Yang[1*]

*Address all correspondence to: yang@mail.nsysu.edu.tw

1 Department of Physics and Center for Nanoscience and Nanotechnology, National Sun Yat-Sen University, Kaohsiung, Taiwan

2 UGC-DAE Consortium for Scientific Research, Mumbai Centre, Bhabha Atomic Research Centre, Trombay, Mumbai, India

References

[1] Chau R, Datta S, Doczy M, Doyle B, Kavalieros J, Metz M. High-k/Metal gate stack and its MOSFET characteristics. IEEE Electron Device Lett 2004;25:408–10.

[2] Lo SH, Buchanan DA, Taur Y, Wang W. Quantum-mechanical modeling of electron tunneling current from the inversion layer of ultra-thin-oxide MOSFETs. IEEE Electron Device Lett 1997;18:209–11.

[3] Homes CC, Vogt T, Shapiro SM, Wakimoto S, Ramirez AP. Optical response of high-dielectric-constant perovskite-related oxide. Science 2001;293:673–6.

[4] Liu J, Duan CG, Yin WG, Mei WN, Smith RW, Hardy JR. Large dielectric constant and Maxwell-Wagner relaxation in $Bi_{2/3}Cu_3Ti_4O_{12}$. Phys Rev B 2004;70:144106(7).

[5] Martín SG, Orrantia AM, Aguirre MH, Franco MÁA. Giant barrier layer capacitance effects in the lithium ion conducting material $La_{0.67}Li_{0.25}Ti_{0.75}Al_{0.25}O_3$. Appl Phys Lett 2005;86:043110(3).

[6] Yang Z, Hou Y, Liu B, Wei L. Structure and electrical properties of Nd_2O_3-doped $0.82Bi_{0.5}Na_{0.5}TiO_3$–$0.18Bi_{0.5}K_{0.5}TiO_3$ ceramics. Ceram Int 2009;35:1423–7.

[7] Wang Z, Chen XM, Ni L, Liu XQ. Dielectric abnormities of complex perovskite $Ba(Fe_{1/2}Nb_{1/2})O_3$ ceramics over broad temperature and frequency range. Appl Phys Lett 2007;90:022904(3).

[8] Raevski IP, Prosandeev SA, Bogatin AS, Malitskaya MA, Jastrabik L. High dielectric permittivity in $AFe_{1/2}B_{1/2}O_3$nonferroelectric perovskite ceramics (A=Ba, Sr, Ca; B=Nb, Ta, Sb). J Appl Phys 2003;93:4130–6.

[9] Wu JB, Nan CW, Lin YH, Deng Y. Giant dielectric permittivity observed in Li and Ti doped NiO. Phys Rev Lett 2002;89:217601(4).

[10] Pecharromán C, Esteban-Betegón F, Bartolomé JF, López-Esteban S, Moya JS. New percolative $BaTiO_3$–Ni composites with a high and frequency-independent dielectric constant ($e_r \approx 80000$). Adv Mater 2001;13:1541–4.

[11] Cohn JL, Peterca M, Neumeier JJ. Low-temperature permittivity of insulating perovskite manganites. Phys Rev B 2004;70:214433(6).

[12] Park T, Nussinov Z, Hazzard KRA, Sidorov VA, Balatsky AV, Sarrao JL, Cheong SW, Hundley MF, Lee JS, Jia QX, Thompson JD. Novel dielectric anomaly in the hole-doped $La_2Cu_{1-x}Li_xO_4$ and $La_{2-x}Sr_xNiO_4$ insulators: signature of an electronic glassy state. Phys Rev Lett 2005;94:017002(4).

[13] Rivas J, Rivas-Murias B, Fondado A, Mira J, Señarís-Rodríguez MA. Dielectric response of the charge-ordered two-dimensional nickelate$La_{1.5}Sr_{0.5}NiO_4$. Appl Phys Lett 2004;85:6224–6.

[14] Zhu WJ, Tamagawa T, Gibson M, Furukawa T, Ma TP. Effect of Al inclusion in HfO_2 on the physical and electrical properties of the dielectrics. IEEE Electron Device Lett 2002;23:649–651.

[15] Mukherjee S, Pal AK, Bhattacharya S, Raittila J. Magnetism of Mn_2O_3 nanocrystals dispersed in a silica matrix: Size effects and phase transformations. Phys Rev B 2006;74:104413(10).

[16] Mukherjee S, Lin YH, Kao TH, Chou CC, Yang HD. Searching for high-k RE_2O_3 nanoparticles embedded in SiO_2 glass matrix. J Appl Phys 2012;111:064103(6).

[17] Sakka S, Kamiya K. The sol–gel transition in the hydrolysis of metal alkoxides in relation to the formation of glass fibers and films. J Non-Cryst Solids 1982;48:31–46.

[18] Krol DM, van Lierop JG. The densification of monolithic gels. J Non-Cryst Solids 1984;63:131–44.

[19] Ankudinov A, Ravel B, Rehr JJ, Newville M. FEFFIT Manual within the FEFF Project (Seattle, WA: University of Washington, USA); 1992–1999.

[20] Mukherjee S, Chen CH, Chou CC, Tseng KF, Chaudhuri BK, Yang HD. Colossal dielectric and magnetodielectric effect in Er_2O_3 nanoparticles embedded in a SiO_2 glass matrix. Phys Rev B 2010;82:104107(7).

[21] Afify ND, Dalba G, Kuzmin A. Local structure around Er^{3+} in SiO_2-HfO_2glassy waveguides using EXAFS. Phys Rev B 2007;76:024114(8).

[22] Maqsood A. Phase transformations in $Er_2Si_2O_7$ ceramics. J Mater Sci Lett 1997;16:837–840.

[23] Losurdo M, Giangregorio MM, Capezzuto P, Bruno G, Toro RG, Malandrino G, Fragalà IL, Armelao L, Barreca D, Tondello E, Suvorova AA, Yang D, Irene EA. Multifunctional nanocrystalline thin films of Er_2O_3: interplay between nucleation kinetics and film characteristics. Adv Funct Mater 2007;17:3607–12.

[24] Chen S, Zhu YY, Xu R, Wu YQ, Yang XJ, Fan YL, Lu F, Jiang ZM, Zou J. Superior electrical properties of crystalline Er_2O_3 films epitaxially grown on Si substrates. Appl Phys Lett 2006;88:222902(3).

[25] Rivas J, Mira J, Rivas-Murias B, Fondado A, Dec J, Kleemann W, Señarís-Rodríguez MA. Magnetic-field-dependent dielectric constant in $La_{2/3}Ca_{1/3}MnO_3$. Appl Phys Lett 2006;88:242906(3).

[26] Jana A, Kundu TK, Pradhan SK, Chakravorty D. Dielectric behavior of Fe-ion-doped $BaTiO_3$ nanoparticles. J Appl Phys 2005;97:044311(6).

[27] Rivera I, Kumar A, Ortega N, Katiyar RS, Lushnikov S. Divide line between relaxor, diffused ferroelectric, ferroelectric and dielectric. Solid State Commun 2009;149:172–6.

[28] Lal HB. Low temperature dielectric studies of some rare-earth oxides. J Phys C: Solid State Phys 1980;13:3969–76.

[29] Yu Z, Ang C, Guo R, Bhalla AS. Ferroelectric-relaxor behavior of $Ba(Ti_{0.7}Zr_{0.3})O_3$ ceramics. J Appl Phys 2002;92:2655–7.

[30] Raymond O, Font R, Suárez-Almodovar N, Portelles J, Siqueiros JM. Frequency-temperature response of ferroelectromagnetic $Pb(Fe_{1/2}Nb_1/_2)O_3$ ceramics obtained by different precursors. Part I. Structural and thermo-electrical characterization. J Appl Phys 2005;97:084107(8).

[31] Ang C, Yu Z, Cross LE. Oxygen-vacancy-related low-frequency dielectric relaxation and electrical conduction in $Bi:SrTiO_3$. Phys Rev B 2000;62:228–36.

[32] Samara GA. The relaxational properties of compositionally disordered ABO_3 perovskites. J Phys: Condens Matter 2003;15:R367–R411.

[33] Scott JF. Ferroelectrics go bananas. J Phys: Condens Matter 2008;20:021001(2).

[34] Pintilie L, Alexe M. Ferroelectric-like hysteresis loop in nonferroelectric systems. Appl Phys Lett 2005;87:112903(3).

[35] Yáñez-Vilar S, Mira J, Sánchez-Andújar M, Castro-García S, Fondado A, Rivas J, Senarís-Rodríguez MA. Particle size reduction: a way to enhanced dielectric properties of magnetocapacitive $La_{2/3}Ca_{1/3}MnO_3$. Appl Phys Lett 2010;96:162904.

[36] Kimura T, Kawamoto S, Yamada I, Azuma M, Takano M, Tokura Y. Magnetocapacitance effect in multiferroic $BiMnO_3$. Phys Rev B 2003;67:180401(R)(4).

[37] Tang J, Feng L, Wiemann JA. Negative magnetoresistance of γ-Fe_2O_3 observed in γ-Fe_2O_3/Ag granular nanocomposite. Appl Phys Lett 1999;74:2522–4.

[38] Catalan G. Magnetocapacitance without magnetoelectric coupling. Appl Phys Lett 2006;88:102902(3).

[39] Mukherjee S, Chen CH, Chou CC, Yang HD. Anomalous dielectric behavior in nanoparticle Eu_2O_3:SiO_2 glass composite system. Euro Phys Lett 2010;92:57010(4).

[40] Kao TH, Mukherjee S, Yang HD. Magnetic nanoparticles induced dielectric enhancement in $(La,Gd)_2O_3$:SiO_2 composite systems. J Magn Magn Mater 2013;346:11–5.

[41] Lukashev P, Sabirianov RF. Flexomagnetic effect in frustrated triangular magnetic structures. Phys Rev B 2010;82:094417(6).

[42] Eliseev EA, Glinchuk MD, Khist V, Skorokhod VV, Blinc R, Morozovska AN. Linear magnetoelectric coupling and ferroelectricity induced by the flexomagnetic effect in ferroic. Phys Rev B 2011;84:174112(16).

[43] Foster AS, Lopez Gejo F, Shluger AL, Nieminen RM. Vacancy and interstitial defects in hafnia. Phys Rev B 2002;65:174117(13).

[44] Nogami M, Moriya Y. Glass formation through hydrolysis of $Si(OC_2H_5)_4$ with NH_4OH andHCl solution. J Non-Cryst Solids 1980;37:191–201.

[45] Rocca F, Ferrari M, Kuzmin A, Daldosso N, Duverger C, Monti F. EXAFS studies of the local structure of Er^{3+} ions in silica xerogel co-doped with aluminium. J Non-Cryst Solids 2001;293–295:112–7.

[46] Kliava J, Malakhovskii A, Edelman I, Potseluyko A, Petrakovskaja E, Melnikova S, Zarubina T, Petrovskii G, Bruckental Y, YeshurunY. Unusual magnetic transitions and nature of magnetic resonance spectra in oxide glasses containing gadolinium. Phys Rev B 2005;71:104406(9).

[47] Kliava J, Malakhovskii A, Edelman I, PotseluykoA, Petrakovskaja E, Melnikova S, Zarubina T, Petrovskii G, Bruckental Y, Yeshurun Y. Reply to "Comment on 'Unusual magnetic transitions and nature of magnetic resonance spectra in oxide glasses containing gadolinium.'" Phys Rev B 2006;74:026404(2).

[48] Bud'ko SL, Canfield PC. Evaluation of a long-time temperature drift in a commercial quantum design MPMS SQUID magnetometer using Gd_2O_3 as a standard. J Magn Magn Mater 2006;299:281–7.

[49] Hadjipanayis G, Sellonyer DJ, Brandt B. Rare-earth-rich metallic glasses. I. Magnetic hysteresis. Phys Rev B 1981;23:3349–54.